Published by IOP Publishing for Sissa Medialab

Received: *June 14, 2019*
Revised: *October 10, 2019*
Accepted: *December 2, 2019*
Published: *January 17, 2020*

3rd European Conference on Plasma Diagnostics (ECPD2019)
6–10 May 2019
Lisbon, Portugal

2020 JINST 15 C01018

Characterization of modified 90° cylindrical energy analyzer with electron beam

R. Sharma,[1] **I.S. Nedzelskiy, A. Malaquias and R. Henriques**

Instituto de Plasma e Fusão Nuclear, Instituto Superior Tecnico, Universidade de Lisboa, Av. Rovisco Pais, 1049-001 Lisboa, Portugal

E-mail: rsharma@ipfn.ist.utl.pt

Abstract: The Heavy Ion Beam Diagnostic (HIBD) installed on the small ISTTOK tokamak is based on Xe^{+} species primary beam injector (E_0 = 25 keV of energy) and a multiple cell array detector (MCAD) of secondary, Xe^{2+}, ions. In this mode of operation, a compact multiple-channel 90° cylindrical energy analyzer (CEA) was proposed. In simulations using SIMION code significant improvements of energy resolution and strong decrease of the angular aberration coefficient due to lensing properties of fringing field were obtained with deceleration of ions inside CEA and detection at decelerating potential. Recently, the simulations have been extended to investigate the influences on the measurements of the CEA housing chamber and the secondary electron emission (SEE) from the deceleration/detector plate.

To shield the electric field perturbations introduced by the chamber, two guard rings (GR) have been added on top and bottom between CEA plates. To overcome the SEE effect, the detector part has been modified by adding two grids and ions detection at zero potential. The GR dimensions and position, and the distances between the grids and detector plate have been optimized by SIMION code.

This paper presents the results of numerical simulations and experiments, obtained with the modified CEA in normal and two-times deceleration modes using electron beam. The energy resolution of $(\Delta E/E_0) \sim 2.4 \times 10^{-3}$ has been demonstrated in deceleration mode insensitive to the $\Delta\theta_{\text{in}} = \pm 1°$ change of the analyzed beam entrance angle. Good agreement between the experimental results and the numerical simulation predictions has been obtained.

Keywords: Detector alignment and calibration methods (lasers, sources, particle-beams); Heavy-ion detectors; Nuclear instruments and methods for hot plasma diagnostics

[1]Corresponding author.

https://doi.org/10.1088/1748-0221/15/01/C01018

Contents

1 Introduction

The HIBD installed on the small ISTTOK tokamak is based on Xe^+ (or Cs^+) species primary beam injector ($E_0 = 25$ keV of energy) and the MCAD that collects the fan of secondary Xe^{2+} (Cs^{2+}) ions created along the primary beam path due to impact with the plasma electrons [1]. In this multichannel mode of operation, the use of standard Proca-Green 30° parallel-plate energy analyzer for the plasma potential and potential fluctuations measurements [2] is of reduced applicability due to the geometrical constraints at HIBD port in ISSTOK. Hence, a compact multiple-channel multi-slit 90° cylindrical energy analyzer (CEA) with combined MCAD and split-plate detection (SPD) was proposed [3]. In simulations using SIMION code significant improvements of energy resolution was obtained with deceleration of ions inside CEA by respective polarization of the potential ψ_0 at the central (standard) radios $R_0 = \frac{1}{2}(R_{out} + R_{in})$ (R_{out}, R_{in} are the outer and inner radii of the CEA plates) and detected at the same decelerating potential. Quantitatively, the improvement of energy resolution is determined by the value of the deceleration coefficient $k_E = (1 - q\psi_0/E_0)^{-1}$ (q is the charge of the analyzed particle) as the beam energy inside CEA is reduced k_E-times ($E_{dec} = E_0/k_E$). Also, a strong decrease of the angular aberration coefficient was demonstrated exploiting lensing properties of fringing field at the beam entrance.

Recently, the simulations have been extended to include the real shape of the CEA housing vacuum chamber and the secondary electron emission (SEE) from the deceleration/detector plate and demonstrate sufficient influence on the CEA operation. The obtained results demanded to some additional elements in the CEA design which have been introduced in a $\frac{1}{2}$-size (of the described in ref. [3]) CEA, constructed and manufactured for the experimental verification of the simulation predictions.

This paper presents the results of numerical simulations and experiments obtained with the modified CEA with SPD detection in normal (not decelerated), $k_E = 1$, and two-times deceleration, $k_E = 2$, operational modes. In this characterization an energy adjustable 2 keV electron beam has been used.

2020 JINST 15 C01018

The paper is organized as follows. In section 2 the vacuum chamber influence and SEE from the deceleration/detector plate are investigated by numerical simulation for the non-modified CEA. The modified CEA is described and characterized by simulations in section 3. The results obtained in experiments on electron beam test facility are presented in section 4. The analysis and comparison with simulation predictions are done in section 5. Summary is given in section 6.

2 Influence of vacuum chamber and SEE from CEA detector plate

The numerical simulations of the vacuum chamber influence and the SEE effect have been performed for a $\frac{1}{2}$-size non-modified 90° CEA with $R_{\text{in}} = 180\,\text{mm}$, $R_{\text{out}} = 210\,\text{mm}$, $H_{\text{CEA}} = 60\,\text{mm}$ of height, $S_{EG} = S_{DG} = 3\,\text{mm}$ of the distances from the CEA plates to respectively entrance slit and deceleration/detection plate. A DN100 CF vacuum 6-way cross chamber guarantees the respective dimensional scaling of the CEA housing. The following simulations were performed in SIMION software (8.0 version) [4] and it showed no effect of space charge on the effective beam trajectory for expected magnitudes of current (hundreds of nA) for HIBD on ISTTOK.

2.1 Effect of electric field perturbations introduced by vacuum chamber

The proximity of vacuum chamber walls determines the disturbance of electric field between the CEA plates, influencing the analyzer operation. That influence on beam transmission inside CEA is demonstrated in figure 1, showing the simulated trajectories and the beam images at the CEA exit of rectangular $4 \times 4\,\text{mm}^2$ uniform parallel electron beam with energies $E_0 = 1.7 \pm 0.1\,\text{keV}$ propagating along the CEA centerline for respectively normal (figure 1a) and deceleration (figure 1b) operational modes (the voltages applied to the CEA are (normal/deceleration): $U_{\text{in}} = +0.44/-0.65$ kV, $U_{\text{out}} = -0.51/-1.05\,\text{kV}$ and $U_{DG} = 0/-0.85\,\text{kV}$ of the voltage applied to the deceleration grid). Where, U_{in} and U_{outer} are the voltages on the inner and outer electrodes, respectively.

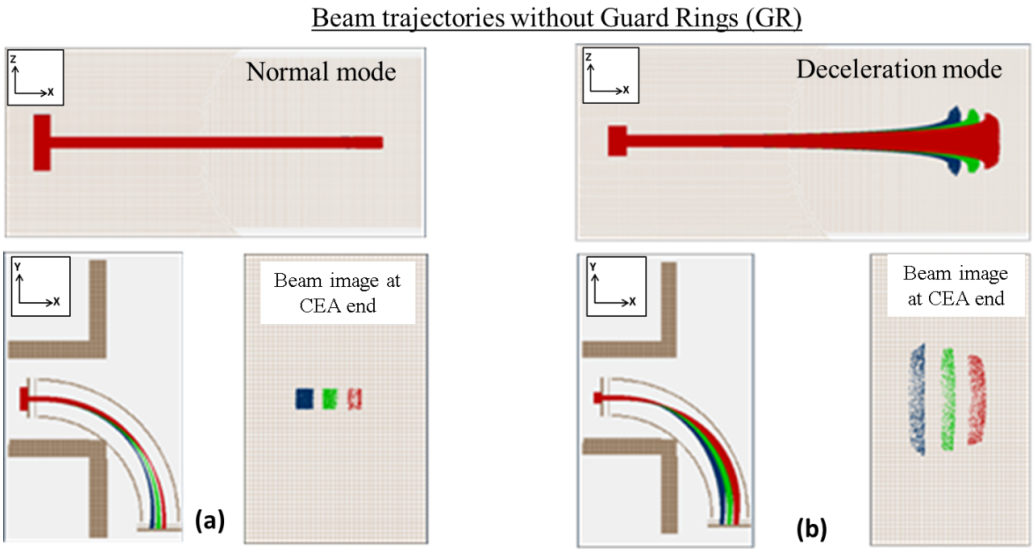

Figure 1. Electron beam trajectories inside and images at the exit of the CEA without guard rings in normal, $\psi_0 = 0\,\text{kV}$ (a), and deceleration, $\psi_0 = -0.85\,\text{kV}$ (b), modes.

2020 JINST 15 C01018

Electron beam trajectories inside CEA in XZ and XY for three beam energies, 1.6 (blue), 1.7 (green), 1.8 (red) keV and the image at the end MCAD with guard rings for (a) normal mode; $\psi_0 = 0$ kV and (b) for the deceleration mode; $\psi_0 = -0.85$ kV.

From figure 1a for normal mode the beam shape and size are unchanged. From figure 1b for deceleration mode a strong effective amplification of the beam size in vertical direction due to the integral-length effect of the electric field distortion between CEA plates introduced by the vacuum chamber is evident. This perturbation effect practically denies the CEA operation in multichannel mode considered in ref. [3], as it implies an effective overlapping of the adjacent channels.

2.2 Secondary electron emission effect

Ref. [3] considers the measurements of beam energy by the current difference between plates of SPD [2] kept at deceleration potential. However, in such detection approach the SEE effect can lead to wrong results independently on whether the CEA is used for the energy analysis of ion or electron beams.

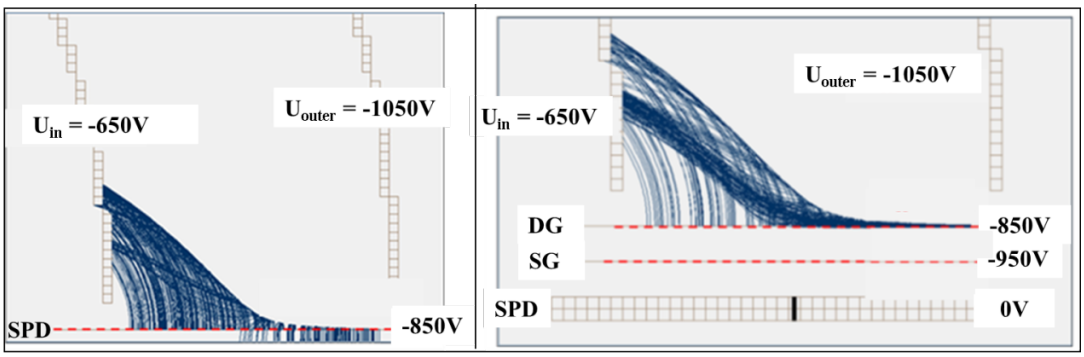

Figure 2. Secondary electrons trajectories from deceleration/detection plate inside non-modified (a) and from deceleration grid of modified (b) CEA at deceleration mode. Where, DG = deceleration grid, SG = SEE suppression grid, SPD = split plate detector.

In figure 2a of non-modified CEA there are shown the trajectories of 5 eV electrons ejected from the surface of deceleration/detection plate when CEA is operating in deceleration mode. From this figure and the respective CEA potentials it is clear that if the analyzed electron beam is completely on the right(high-energy) or left (low energy) sides, the secondary electrons will be respectively retarded or collected by the CEA outer or inner plates and the detected signal between right-left plates will differ. Obviously, if the analyzed beam partially occupies both regions near the centerline, the measurements with SPD centered at the same position will be incorrect. Similar properties also characterize the normal mode of CEA operation.

3 Modified CEA

The design of the modified CEA to exclude the above mentioned obstructive effects is schematically shown in figure 3. The entrance part of CEA presents 16 (vertical) × 30 (horizontal) mm^2 window (1) covered by grid (EG). The CEA plates (2) are aluminum of 1 mm thickness. There are two (top and bottom) additional electrodes (guard rings (GR)) (3) to shield from housing chamber disturbance.

2020 JINST 15 C01018

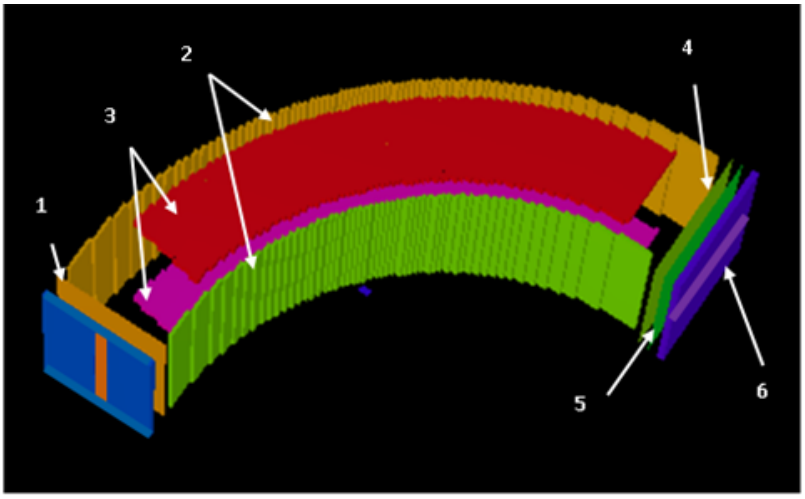

Figure 3. Arrangement and additional elements of the modified CEA presented in SIMION software. The numeric in the picture corresponding to respective CEA elements are as following: (1) Entrance grid (EG), (2) inner and outer CEA plates, (3) top and bottom guard rings, (4) Deceleration grid (DG), (5) SEE suppression grid (SG) and (6) split plate detector.

The GR are made from copper plate 1.5 mm of thickness, 26 mm of the radial width and inserted on 2 mm inside between the CEA plates. The GR do not cover the whole 90° sector of the CEA (GR azimuth angle is $\varphi = 70°$) keeping the gaps of $\varphi = \pm 10°$ at the entrance and exit. Such arrangement resulted from optimized in numerical simulations CEA operation with improved angle aberration characteristic exploiting the lensing effect of fringing field [3]. Though the introduced GR just changes the source of electric field perturbations, these perturbations can be controlled by manipulation of the voltage applied to GR [5]. To overcome the SEE effect, the detector is changed by adding two grids: deceleration grid (4) (DG) and SEE suppression grid (5) (SG). The SPD (6) is 5 mm of height in vertical direction and arranged in the CEA equatorial middle-plane. It is kept at zero potential. In such modified configuration of the detector part, applying the potential on the SG more negative than on DG, the SEE effect influence is completely avoided as demonstrated in figure 2b. In addition, a phosphor screen (PS) $30 \times 60\,\mathrm{mm}^2$ of dimensions is placed between the SG and SPD. There is 5 (vertical) $\times$ 30 (horizontal) mm^2 opened window in PS to allow the beam transmission to the SPD. All grids are tungsten and have 40% of transparency. The GR dimensions and arrangement, distances between the grids and detector plate have been optimized in numerical simulation by SIMION code.

Simulations, as those presented in figure 1, have been performed for the modified CEA in normal and deceleration modes. The respective results for the GR potentials $U_{GR} = 0\,\mathrm{V}$ in normal mode and $U_{GR} = -0.85\,\mathrm{kV}$ in deceleration mode (equal to the potentials on DG) are shown in figure 4. From figure 4a for normal mode the beam size is slightly elongated in vertical direction. From figure 4b for deceleration mode the beam size in vertical direction is almost unchanged, while, in similarity with the results of ref. [3], there is an effective magnification of beam size in horizontal (energy dispersion) direction.

Electron beam trajectories inside CEA in XZ and XY for three beam energies, 1.6 (blue), 1.7 (green), 1.8 (red) keV and the image at the end MCAD with optimized voltage on the guard rings for (a) normal mode; $\psi_0 = 0\,\mathrm{kV}$ and (b) for the deceleration mode; $\psi_0 = -0.85\,\mathrm{kV}$.

2020 JINST 15 C01018

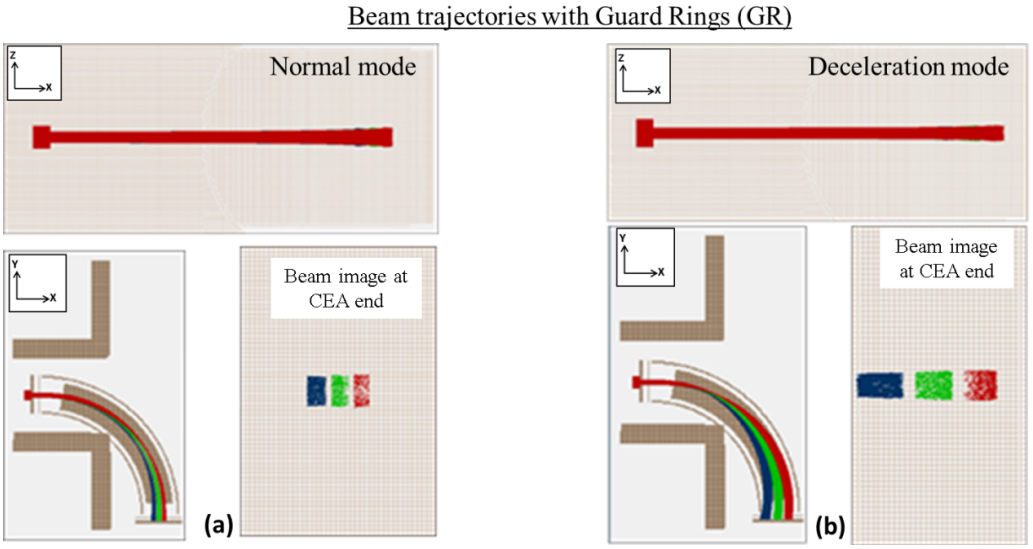

Figure 4. Electron beam trajectories inside and images at the exit of the CEA with guard rings in normal, $\psi_0 = 0$ kV (a), and deceleration, $\psi_0 = -0.85$ kV (b), modes.

4 Test experiments with modified CEA

The experiments with modified CEA have been performed on test facility with strip-shape electron beam extracted from electron source by $0.3 \times 12\,\text{mm}^2$ slit. The CEA is fixed inside 6-way cross vacuum chamber with the entrance window located at 100 mm from the extraction electrode of the electron source. The extraction slit is oriented vertically relative to the energy dispersion direction of CEA. The mounting of the electron gun to the 6-way cross vacuum chamber allowed for $\Delta\theta_{\text{in}} \sim \pm 1^\circ$ adjustment of the input beam angle at the CEA entrance.

The electron beam geometrical characteristics at the CEA entrance have been investigated by visual observation of beam image on removable phosphor screen arranged in front of CEA. The observed image indicates a beam size of 4 mm in horizontal (energy dispersion) direction and 16 mm in vertical (extraction slit orientation) direction with $\sim \pm 1^\circ$ divergence. The use of strip-shape electron beam allows the simultaneous visual control of the beam shape on PS in vertical direction beyond the 5 mm of the SPD height borders at the CEA exit.

Figure 5 presents the observed on phosphor screen and simulated images of $4 \times 16\,\text{mm}^2$ uniform electron beam with $\pm 1^\circ$ divergence in horizontal and vertical directions for the beam energies of $E_0 = 1.7 \pm 0.1$ keV in normal mode and $U_{GR} = 0$ V. Considering the tolerances of CEA fabrication, assembling and installation (that are not counted in SIMION simulations), the data in figure 5 show

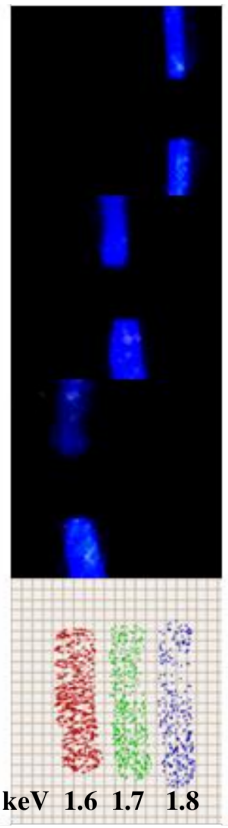

Figure 5. Observed on phosphor screen and simulated images of electron beam.

2020 JINST 15 C01018

that the beam position, determined by beam energy and beam dimensions are in reasonably good agreement with simulations. There is no influence of the variation of the beam entrance angle on the beam image at the analyzer end for available $\Delta\theta_{\text{in}} \sim \pm 1^{\text{o}}$at fixed beam energy as also predicted by the simulations. The effective input angle variation of the beam in HIBD experiment in ISSTOK is expected to be $\Delta\theta_{\text{in}} \sim \pm 0.5^{\text{o}}$ [6].

The first order dispersion relation for the 90° CEA and the effective split-plate current-to-energy change characteristic (I-E characteristic) are [3]:

$$\Delta r/R_0 = C_\theta \Delta\theta_{\text{in}} + k_E C_E \Delta E/E_0 \tag{4.1}$$

$$\delta i = k_E C_E (w_b/2R_0)^{-1} \Delta E/E_0 (\Delta\theta_{\text{in}} = 0) \tag{4.2}$$

where $\Delta r/R_0$ is the normalized initial position of the ion relative to standard trajectory at the analyzer entrance, C_θ is the first-order angular aberration coefficient, $\Delta\theta_{\text{in}}$ is the angle of beam trajectory relative to the standard trajectory, C_E is the first order energy dispersion coefficient and $\Delta E/E_0$ is the normalized ion energy and w_b is beam width at the input of the analyzer.

From eq. (4.2), the I-E characteristic depends on the beam width in energy dispersion direction, and, for the same beam widths, it should have steeper slope in deceleration mode. The slope of the I-E characteristic designates the energy resolution, $(\Delta E/E_0)_{\text{res}}$, being k_E-times better in deceleration mode for the unaltered minimal resolved current δi_{min}. For the k_E-times decelerated beam, or a non-decelerated beam with k_E-times lower initial energy, the I-E characteristics should coincide. Also, the I-E characteristics should saturate at $\delta i = \pm 1$ when the beam is completely on one of the split plates, hitting the limit of the dynamic range of the measurements.

Figure 6 shows the I-E characteristics obtained for the beam energies of $E_0 = 1.8$ keV (B) and $E_0 = 0.9$ keV (C) in normal mode, and for the beam energy of $E_0 = 1.8$ keV in deceleration (D) ($E_{\text{dec}} = \frac{1}{2}E_0 = 0.9$ keV) mode. The beam width in energy dispersion direction have been maintained at $w_b = 4$ mm by manipulation of the voltage applied to the GR [5]. The respective CEA voltages are specified in table 1. The ΔU on the X axis refers to the change in beam energy in electron volts from the reference value for respective configurations: B, C and D (as mentioned in the graph).

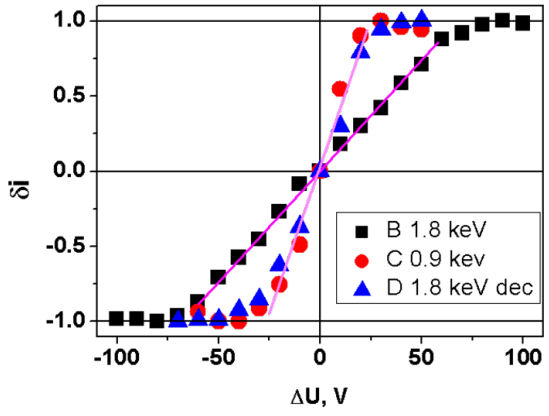

Figure 6. Split-plate I-E characteristics in normal and deceleration modes. B (black squares) and C (red circles) refers to normal mode operation with $E_0 = 1.8$ keV and 0.9 keV, respectively and D (blue triangles) refers to the deceleration mode ($k = 2$). The voltages specification for the 3 cases is presented in table 1.

2020 JINST 15 C01018

Table 1. Voltages applied to the CEA electrodes. Where U_{in} and U_{out} is the voltage applied on the inner and outer curve plate of the analyzer, respectively. U_{DG}, U_{SG} and U_{GR} are the voltage on deceleration grid, SEE suppression grid and pair of guard rings, respectively. ψ_0 is the mean potential at the central line trajectory.

Reference in figure 6	E_0 keV	U_{in} kV	U_{out} kV	U_{DG} kV	U_{SG} kV	U_{GR} kV	ψ_0 kV
B	1.8	+0.470	−0.540	0	−0.2	0	0
C	0.9	+0.240	−0.270	0	−0.2	0	0
D	1.8 (deceleration)	−0.650	−1.150	−0.9	−1	−0.72	−0.9

Results presented in figure 6 completely confirm the expected features of the I-E characteristics and demonstrate the principle of the k_E-times energy resolution improvement by deceleration of the analyzed beam inside the CEA.

5 Analysis and comparison with simulations

Energy dispersion. Estimation of the energy dispersion, $\Delta r/\Delta E$, from the beam shifts in figure 5 gives the value of $\Delta r/\Delta E \sim 0.05$ mm/V. From eq. (4.1) and $\Delta\theta_{\text{in}} = 0$, the value of energy dispersion coefficient C_E can be estimated, giving $C_E = 0.81$ for $k_E = 1$ (normal mode), $R_0 = 105$ mm and $E_0 = 1.7$ keV. The simulations by SIMION code give the values of $C_E = 0.78$ and $C_E = 0.83$ for the respectively normal and deceleration modes (table 2). All the obtained C_E values are within $\sim 3\%$ of the theoretical value $C_E = 0.8$ [3].

Table 2. Dispersion coefficient for angle (C_θ) and energy (C_E) for normal and deceleration mode.

	Normal ($k_{\text{e}} = 1$)	Deceleration ($k_{\text{e}} = 2$)
C_θ	0.2	0.04
C_E	0.78	0.83

Energy resolution. Eq. (4.2) gives the value of $\delta i_{\text{min}} \sim 0.2$ (limitation due to power supply, $\Delta U > 10$ eV) as reliable current difference resolution in experiment with electron beam and figure 6 provides the calibration. For $w_b = 4$ mm, $R_0 = 105$ mm, $C_E = 0.8$, eq. (4.2) gives $(\Delta E/E_0)_{\text{res}} \sim 4.8\times10^{-3}$ and 2-times better, $(\Delta E/E_0)_{\text{res}} \sim 2.4\times10^{-3}$, energy resolutions in normal and deceleration modes, respectively.

Angle aberration. Simulations by SIMION code give $C_\theta = 0.2$ and $C_\theta = 0.04$ for the angle aberration coefficient in respectively normal and deceleration modes. From eq. (4.1), the equivalent of effective energy change due to angle aberration can be estimated by equating $\Delta r/R_0 = 0$. It gives respectively $(\Delta E/E_0)_\theta = 4.3\times10^{-3}$ and $(\Delta E/E_0)_\theta = 4.3\times10^{-4}$ in normal and deceleration modes for $\Delta\theta_{\text{in}} = 1^\circ$ of the experiments entrance angle variation range. The obtained values of $(\Delta E/E_0)_\theta$ are within the respective values of energy resolution, $(\Delta E/E_0)_{\text{res}}$, in normal and deceleration modes and explain the experimental observations of the respectively weak and the absence of sensitivity to the change of beam entrance angle inside the experimentally available range.

2020 JINST 15 C01018

6 Summary

The modified 90° cylindrical electrostatic energy analyzer has been investigated both numerically and in experiments with electron beam in real operational conditions. A reasonably good agreement between the experimental results and the numerical simulation predictions is observed. It has been shown that introduction of top-bottom guard rings between CEA plates and modification of the detector part by adding two biased grids (the decelerating and SEE suppressing) and detector at zero potential, solves the problem caused by the electric field perturbation by the walls of vacuum chamber and SEE influence on the CEA operation. Furthermore, keeping the detector at zero potential simplifies the detection electronics. The CEA operation in deceleration mode has been demonstrated and confirmed experimentally. The energy resolution of $(\Delta E/E_0)_{\text{res}} \sim 2.4 \times 10^{-3}$ has been obtained in $k_E = 2$ deceleration mode of operation insensitive to the change of the analyzed beam entrance angle in the range of $\Delta\theta_{\text{in}} = \pm 1°$. The presented modified 90° cylindrical electrostatic energy analyzer will be applied for the plasma potential and potential fluctuations [7] measurements by HIBD on the ISTTOK tokamak. For double-charged ($q = 2$) secondary ions, the energy resolution of $(\Delta E/E_0)_{\text{res}} \sim 10^{-3}$ (20 V of absolute value for the 20 keV of diagnostic beam energy) is expected in $k_E = 5$ ($\psi_0 = 8$ kV) deceleration mode of the CEA operation.

Acknowledgments

IPFN activities received financial support from "Fundação para a Ciência e Tecnologia" through project UID/FIS/50010/2019.

References

[1] J.A.C. Cabral, A. Malaquias, A. Praxedes, W. Van Toledo and C.A.F. Varandas, *The heavy ion beam diagnostic for the tokamak ISTTOK*, *IEEE Trans. Plasma Sci.* **22** (1994) 350.

[2] L. Solensten and K.A. Connor, *Heavy ion beam probe energy analyzer for measurements of plasma potential fluctuations*, *Rev. Sci. Instrum.* **58** (1987) 516.

[3] I.S. Nedzelskiy et al., 90° *cylindrical analyzer for the plasma potential fluctuations measurements by heavy ion beam diagnostic on the tokamak ISTTOK*, *Fusion Eng. Des.* **123** (2017) 897.

[4] https://simion.com/info/simion80.html.

[5] I.S. Nedzelskiy, R. Sharma and A. Malaquais, *Double-focusing properties of electrostatic cylindrical deflector with additional electrodes*, to be submitted for publication.

[6] A. Malaquias et al., *Evolution of the poloidal magnetic field profile of the ISTTOK plasma followed by heavy ion beam probing*, *Fusion Eng. Des.* **34-35** (1997) 671.

[7] A.V. Melnikov, *Electric potential in toroidal plasmas*, Springer Nature AG, Switzerland (2019) [DOI].

2020 JINST 15 C01018